

Gradient-based Source Mask Optimization for Extreme Ultraviolet Lithography

Xu Ma, *Senior Member, IEEE*, Zhiqiang Wang, Xuanbo Chen, Yanqiu Li, and Gonzalo R. Arce, *Fellow, IEEE*

Abstract—Extreme ultraviolet (EUV) lithography is the most promising technology for next generation very-large scale integrated circuit fabrication. EUV lithography invariably introduces distortions in the projected lithographic mask patterns and thus inverse lithography tools are needed to compensate for these. This paper develops two kinds of model-based source and mask optimization (SMO) frameworks, referred to as the parametric SMO and the pixelated SMO, both to provide primary strategies for improving the image fidelity of EUV lithography. In the parametric SMO, the source pattern is defined by a few geometrical parameters. Meanwhile, in the pixelated SMO, the light source is represented by a grid pattern. These two SMO frameworks are established using a nonlinear imaging model that coarsely approximates the optical proximity effect, flare and photoresist effects in an analytic closed-form. In addition, a retargeting method is used to approximately compensate for the mask shadowing effects based on a calibrated shadowing model. Another contribution of this paper is to develop a hybrid cooperative optimization algorithm based on conjugate gradient and compare it to the simultaneous SMO algorithm. It is shown that the hybrid SMO algorithm can achieve superior convergence characteristics and computational efficiency over the simultaneous SMO algorithm.

Index Terms—Computational lithography, inverse problem, EUV lithography, source and mask optimization (SMO).

I. INTRODUCTION

OPTICAL lithography is extensively used in very-large scale semiconductor fabrication. Optical lithography systems expose the underlying wafer by a pre-defined mask pattern and then print out the semiconductor devices on the wafer. As the critical dimension (CD) of integrated circuits shrinks below 22nm, extreme ultraviolet (EUV) lithography with 13.5nm illumination wavelength has become one of the most prospective alternative to deep ultraviolet (DUV) lithography with 193nm wavelength [1]. Although the much shorter wavelength of EUV lithography greatly pushes the resolution limit, all materials are strong absorbers of EUV light [2], [3]. Thus, EUV lithography systems are designed based on all-reflective optics with off-axis illuminations. As shown in Fig. 1, the illumination emits the EUV light rays

that expose the mask with about 6° incidence angle. The EUV mask is composed of Mo/Si multilayers, some of which are coated by absorbers. The mask regions covered by absorbers will absorb most of the EUV light, while the mask regions without absorbers will reflect most of the EUV light into the projector optics. The projector optics is used to project the layout pattern from the mask onto the wafer. After the development of photoresist, the layout pattern will be printed on the wafer. In general, a nonlinear mathematical model can be used to describe the imaging process of EUV lithography systems, where the inputs include the source, mask and other lithographic parameters, and the output is the print image on the wafer.

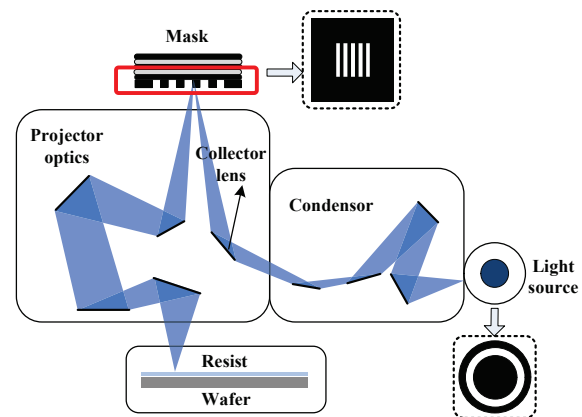


Fig. 1. The sketch of EUV lithography system. The light source emits the EUV light rays that pass through the condensor and expose the mask. Then, the projector optics transfers the layout patterns from the mask onto the wafer.

In EUV lithography systems, several noticeable effects adversely impact the imaging performance, such as the optical proximity effect (OPE), flare, photoresist and mask shadowing effects [2],[4]-[6]. In this case, computational lithography can be used to compensate for these effects and further improve the imaging resolution and fidelity [7], [8]. Computational lithography encompasses a set of mathematical and algorithmic approaches based on lithographic imaging models to individually or jointly optimize the parameters in lithography systems and development processes. As an important computational lithography method, source and mask optimization (SMO) co-optimizes the source and mask patterns to get much higher degree of optimization freedom compared to the individual source optimization and the optical proximity correction (OPC) that only optimizes the mask [9], [10]. In the past, SMO methods for DUV lithography have been extensively studied and proved to successfully achieve finer resolvable patterns

We thank the financial support by Beijing Natural Science Foundation (4173078), the National Natural Science Foundation of China (Grant No. 61675021 and Grant No. 61675026), and National Science and Technology Major Project. We also thank Mentor Graphics Corporation for providing academic use of Calibre. (*Corresponding authors: Xu Ma and Zhiqiang Wang.*)

X. Ma, Z. Wang, X. Chen and Yanqiu Li are with the Key Laboratory of Photoelectronic Imaging Technology and System of Ministry of Education of China, School of Optics and Photonics, Beijing Institute of Technology, Beijing, 100081, China.

G. R. Arce is with the Department of Electrical and Computer Engineering, University of Delaware, Newark, DE, 19716, USA.

at 45nm-22nm technology nodes and beyond. However, SMO for EUV lithography is still an emerging technique, and the relevant research is ongoing so far. It is important to generalize or apply some instructive ideas of DUV SMO approaches to EUV lithography.

In general, SMO methods can be classified into two branches, one of them is based on parametric source model, and the other is based on pixelated source model. The parametric source model uses several parameters to define the regular source shapes such as circular, annular, quadrapole sources, and so on. On the other hand, the pixelated source is represented by a freeform grid pattern with each pixel corresponding to one point source. The pixelated source introduces much higher degree of optimization freedom than the parametric source, thus is beneficial to further improve the lithography image fidelity. However, the pixelated source model is inevitable to increase the complexity of the optimized source patterns, and increase the runtime of SMO algorithms due to the high-dimensional variables to be optimized. Hereafter, we refer to the SMO methods based on these two source models as parametric SMO and pixelated SMO, respectively. In 2002, Rosenbluth, et al. first introduced the idea of the source and mask co-optimization [11]. Then, the SMO techniques for DUV lithography systems were rapidly developed [12]-[15]. Especially after the invention of freeform diffractive optical elements (DOE) and micro-mirror array, the pixelated SMO methods were proposed and realized in practice [16]-[24],[10]. Subsequently, the SMO methods were extended to incorporate the polarization and pupil wavefront as additional optimization variables to achieve better imaging performance [25]-[28].

Most of these methods mentioned above were developed based on the DUV lithography systems. Recently, Fühner, et al. proposed a parametric SMO approach for EUV lithography based on genetic algorithm to pursue the best overlapping process window and reduce the placement error [29]. However, the degree of optimization freedom in this approach is limited by a set of parameters, such as mask feature sizes, mask absorber parameters, and center radius and latitude of annular illumination. Furthermore, although the genetic algorithm is apt to achieve global optimum, it is sometimes too computationally intensive to solve for a large scale optimization problem. Evanschitzky, et al. proposed an efficient three dimensional EUV mask simulation model for SMO based on the waveguide method and decomposition technique [30]. Liu, et al. proposed a new EUV SMO approach for 7nm technology node and beyond, which enabled the pixelated illumination optimization by using the “FlexPupil” [31]. However, the details of the SMO algorithm was not discussed at length in [31]. Hsu, et al. demonstrated how to use the ASML Brion Tachyon NXE SMO to improve the image log slope and reduce the line edge roughness [32]. Kim, et al. used the ASML Brion’s SMO tool and other resolution enhancement techniques to optimize and extend single exposure bi-directional patterning for 7nm and beyond logic designs [33]. Crouse, et al. used the “Design Intent” approach to guide the EUV source mask co-optimization, which can achieve superior lithographic results more quickly than only using the typical iterative approach [34]. However, these works mentioned above rely on the

current commercial software.

This paper develops two kinds of inverse SMO frameworks, referred to as the parametric SMO and pixelated SMO, based on a coarsely approximate closed-form imaging model that takes into account the OPE, flare and photoresist effects in EUV lithography systems. Subsequently, a retargeting method is proposed to provide a first approach to compensate for the mask shadowing effects based on a calibrated shadowing model. The imaging model used in this manuscript is a coarse approximation to a real EUV lithographic model. The development of more accurate yet mathematically tractable EUV models is an active area of research, as is their use in SMO optimization. Both of the parametric and pixelated SMO problems are formulated as the inverse imaging problems to pursue the optimal source and mask patterns according to the target layouts. The optimization cost function is established based on the Euclidean distance between the target layout and the actual print image. For the parametric SMO, the source variables to be optimized are the outer partial coherence factor and the ring width of annulus. For the pixelated SMO, the intensities of all source pixels can be optimized. On the other hand, we use the block-based method to optimize the mask pattern, where the mask is composed by a set of overlapped basis blocks to reduce the complexity of mask patterns [5], [35].

In order to effectively reduce the image distortion and improve the convergence property, we design a hybrid cooperative optimization algorithm to solve for the SMO problems. The hybrid SMO (HSMO) flow includes two successive steps, i.e., the individual source optimization step and the simultaneous SMO (SISMO) step [22]. The conjugate gradient algorithm is used to iteratively update the source and mask variables during the optimization process. The proposed SMO methods are verified based on the test layouts with 22nm and 16nm critical dimensions. In addition, we investigate and compare four kinds of SMO algorithms, namely the parametric SISMO, parametric HSMO, pixelated SISMO and pixelated HSMO, respectively. It will be shown that the parametric SMO algorithms lead to shorter runtime and manufacture-friendly conventional source shapes, while the pixelated SMO algorithms can further improve the lithography image fidelity by increasing the degree of optimization freedom. In addition, the HSMO algorithms outperform the SISMO algorithms in both of the convergence characteristics and computational efficiency. Note that this paper aims at developing general model-based EUV SMO methods, and comparing different SMO optimization algorithms. More research is also needed in the future to incorporate more rigorous models that fully characterize the EUV SMO problem.

The remainder of this paper is organized as follows. The imaging model of EUV lithography system is briefly described in Sec. II. The mask and source models used for SMO are described in Sec. III. The SMO problems for EUV lithography are formulated in Sec. IV. The gradient-based SMO algorithms are developed in Sec. V. The simulations and analysis are presented in Sec. VI. Section VII provides the conclusions.

II. IMAGING MODEL OF EUV LITHOGRAPHY SYSTEM

Let $\mathbf{J} \in \mathbb{R}^{N_s \times N_s}$ denote the source pattern with each entry representing the intensity of the corresponding source point. $\mathbf{M} \in \mathbb{R}^{N \times N}$ denotes the mask pattern with each entry representing the corresponding reflectivity. \mathbb{R} represents the real number space, N_s and N are the lateral sizes of the source and mask patterns, respectively. Considering the OPE, flare and photoresist effects, the aerial image exposed on the wafer can be formulated as [5], [36]

$$\mathbf{I}_r = \frac{1}{J_{sum}} \sum_{x_s} \sum_{y_s} \left\{ \mathbf{J}(x_s, y_s) \cdot \left[\mathbf{H}_r \otimes |\mathbf{H}^{x_s y_s} \otimes (\mathbf{B}^{x_s y_s} \odot \mathbf{M})|^2 \right] \right\}, \quad (1)$$

where \odot is the entry-by-entry multiplication, \otimes is the convolution operation, (x_s, y_s) is the normalized spatial coordinate on the source plane, and the superscript “ $x_s y_s$ ” refers to the variables corresponding to the source point at (x_s, y_s) . $\mathbf{B}^{x_s y_s} \in \mathbb{R}^{N \times N}$ is the matrix representing the oblique incidence effect, which can be calculated according to the constant scattering coefficient assumption [37]. Although the constant scattering coefficient assumption is an approximation for state-of-the-art EUV systems, it provides an approximation of the mask near field. More precise solutions can be achieved by involving more rigorous mask models. $\mathbf{H}^{x_s y_s}$ is the point spread function (PSF) of the lithography projector, and $J_{sum} = \sum_{x_s} \sum_{y_s} \mathbf{J}(x_s, y_s)$ is a normalization factor. \mathbf{H}_r is the convolution kernel to represent the flare and photoresist effects, which can be calculated as [38], [2], [4], [5]

$$\mathbf{H}_r = [(1 - TIS) \cdot \delta(\vec{r}) + \mathbf{PSF}_f(\vec{r})] \otimes \mathbf{PSF}_r(\vec{r}), \quad (2)$$

where $\vec{r} = (x_w, y_w)$ is the coordinate on the wafer, TIS is the total integrated scatter that can be obtained by integrating over the scattered light in all possible directions, and $\delta(\vec{r})$ is the Dirac’s delta function. In Eq. (2), $\mathbf{PSF}_f(\vec{r})$ is the flare PSF given by [38], [2]

$$\mathbf{PSF}_f(\vec{r}) = \begin{cases} \frac{K}{|\vec{r}|^{n_f+1}} & \text{for } |\vec{r}| > r_{min} \\ 0 & \text{otherwise} \end{cases}, \quad \text{and } K = \frac{1}{2\pi} (n_f - 1) \cdot TIS \cdot r_{min}^{n_f-1}, \quad (3)$$

where n_f is the spectral index, r_{min} is the boundary between the low-frequency phase errors modeled by lens aberrations and the high-frequency phase errors modeled as flare. In Eq. (2), $\mathbf{PSF}_r(\vec{r})$ is the photoresist PSF given by [4]

$$\mathbf{PSF}_r(\vec{r}) = \frac{1}{\sigma_p \sqrt{2\pi}} \exp\left(-\frac{|\vec{r}|^2}{2\sigma_p^2}\right), \quad (4)$$

where σ_p is the standard deviation that varies for different types of photoresists. After the development of photoresist, the print image on the wafer can be calculated as a hard threshold version of the aerial image, such that:

$$\mathbf{Z}(r) = \Gamma\{\mathbf{I}_r - t_r\}, \quad (5)$$

where \mathbf{I}_r is described in Eq. (1), and t_r is the photoresist threshold. $\Gamma\{\bullet\} = 1$ if the argument is larger than 0, otherwise,

$\Gamma\{\bullet\} = 0$. Since $\Gamma\{\bullet\}$ is indifferentiable, we use the sigmoid function to approximate it [39], [40]. The sigmoid function is

$$\text{sig}(x, t_r) = \frac{1}{1 + \exp[-a(x - t_r)]}, \quad (6)$$

where a is the steepness index. Then, Eq. (5) is transformed into

$$\mathbf{Z}(r) = \text{sig}\{\mathbf{I}_r, t_r\}. \quad (7)$$

It is noted that the imaging model mentioned above does not include the mask shadowing effect. However, the oblique incidence of EUV light rays and the thickness of absorbers on the mask will induce pronounced mask shadowing effect, especially when the critical dimension is below 22nm [6], [41]. The mask shadowing will introduce CD bias and shift in the print image. In the following, the calibrated model proposed in [6] is adopted as an example to coarsely approximate the mask shadowing effect. Other mask shadowing models can also be used in the proposed SMO frameworks. More research, however, is needed to attain a more accurate and realistic model of the mask shadowing effect in EUV lithography, which can be used in SMO optimization. The principle of this calibrated model is illustrated in Fig. 2. As shown in Fig. 2(a), the red dashed line and black solid line represent the contours of the target layout and the print image of target layout. According to [6], the mask shadowing effect will introduce a shadowing width B along the contour of print image, where the parameter B can be calibrated based on experimental data. Inspired by the perspective geometry, the shadowing width B can be modelled as

$$B = B_m \cos^{n_s} \alpha_s, \quad (8)$$

where B_m and n_s are calibrated parameters, and α_s can be calculated as

$$\alpha_s = \alpha'_s + \arcsin\left[\left(\frac{2}{W} \sin \frac{F}{2}\right) y\right] \approx \alpha'_s + \left(\frac{2}{W} \sin \frac{F}{2}\right) y, \quad (9)$$

where α'_s is the orientation angle of pattern edge with respect to the coordinate in Fig. 2(c). The origin of the coordinate is at the center of exposure field, and the X, Y and Z axes are shown in Fig. 2(c). In Eq. (9), W is the width of the exposure field, F is the open angle of the ring slit in the exposure field, and y is the y-coordinate of the evaluation point.

In EUV lithography systems, the incidence angle of the light rays onto the mask is about 6° and the secondary azimuth varies across the exposure ring slit. This oblique incidence induces the asymmetric shadowing effect, thus the shadowing width B is not balanced on the near side and far side. As shown in Fig. 2(d), the near side refers to the pattern edge more close to the light source, while the far side refers to the opposite pattern edge. If the incident light ray hits the near side of a pattern, then α_s in Eq. (9) is larger than 90° . If the incident light ray hits the far side, then α_s is smaller than 90° . To account for the asymmetric shadowing effect on different sides, Eq. (8) was separated into two cases

$$B_n = B_{n,m} \cos^{n_s} \alpha_s, \quad B_f = B_{f,m} \cos^{n_s} \alpha_s, \quad (10)$$

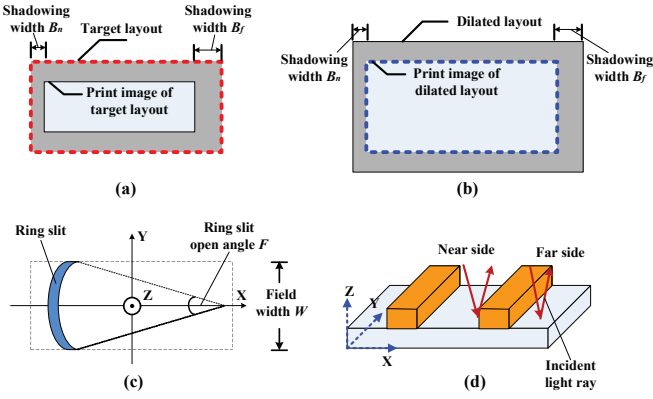


Fig. 2. (a) The mask shadowing effect, (b) the retargeting method to compensate for the mask shadowing effect, (c) the coordinate and parameters in the exposure field, and (d) the near side and far side of the mask pattern [5].

where $B_{n,m}$ and $B_{f,m}$ are the maximum shadowing widths on the near side and far side, respectively. $B_{n,m}$, $B_{f,m}$ and n_s are all parameters that can be calibrated.

Due to the length limit, this paper does not consider other characteristic effects in EUV lithography systems, such as non-telecentricity, pitch-dependent image displacement and so on. Attributed to the off-axis illumination, the non-telecentricity of EUV lithography system induces the pattern displacement with respect to the design, and the amount of displacement is related to the pattern density and defocus value [42], [43]. In principle, these effects may be included into the imaging model by calibrated parameters, and then compensated by the retargeting method or the inverse optimization method.

III. MASK AND SOURCE MODELS USED IN SMO ALGORITHMS

In order to preserve the mask manufacturability, we need to reduce the geometrical complexity of the mask pattern, especially eliminating any singular pixels on the mask. To achieve this goal, we model the mask pattern as the superposition of several overlapped basis blocks [35], [5]. The mask \mathbf{M} in Eq. (1) is formulated as

$$\mathbf{M} = (n_r - n_a) \cdot [\Gamma(\mathbf{W}_M \otimes \Theta_M - 1) + \Gamma(\mathbf{W}_S \otimes \Theta_S - 1)] + n_a, \quad (11)$$

where $n_r \in [0, 1]$ and $n_a \in [0, 1]$ are the reflectivities of the multilayers and absorbers on the EUV mask, respectively. $\mathbf{W}_M \in \mathbb{R}^{N_M \times N_M}$ and $\mathbf{W}_S \in \mathbb{R}^{N_S \times N_S}$ represent the basis blocks of the main features (MF) and sub-resolution assist features (SRAF), respectively. All entries of \mathbf{W}_M and \mathbf{W}_S are equal to 1. N_M and N_S are the lateral sizes of \mathbf{W}_M and \mathbf{W}_S , respectively. $\Theta_M \in \mathbb{R}^{N \times N}$ and $\Theta_S \in \mathbb{R}^{N \times N}$ are the binary matrices with all entries equal to 0 or 1. The one-valued entries of Θ_M and Θ_S indicate the locations of the basis blocks \mathbf{W}_M and \mathbf{W}_S , respectively. It is noted that EUV mask effects have a complex impact on EUV lithography imaging, as extensively studied in the past [44], [45], [46]. The simple mask model in Eq. (11) does not consider the angular response of the multilayer blank. In practice, however,

the reflectivity and phase of the reflected EUV light may vary with the illumination direction. In order to derive the gradient-based SMO algorithms, this paper assumes constant reflectivity, and represents the mask shadowing effect by the calibrated model. During the optimization process, we replace the hard threshold function $\Gamma\{\bullet\}$ in Eq. (11) by the differentiable sigmoid function in Eq. (6) with $t_r = 1$ [35], [5]. Thus, Eq. (11) is transformed into

$$\mathbf{M} = (n_r - n_a) \cdot [\text{sig}(\mathbf{W}_M \otimes \Theta_M, 1) + \text{sig}(\mathbf{W}_S \otimes \Theta_S, 1)] + n_a. \quad (12)$$

The proposed SMO methods optimize Θ_M and Θ_S instead of mask pixels to enforce the minimum mask opening sizes to be larger than the dimensions of basis blocks.

As mentioned above, this paper investigates the SMO methods based on both of the parametric and pixelated source models. Hereafter, those two kinds of SMO methods are referred to as the parametric SMO and pixelated SMO, respectively. The parametric SMO methods constrain the source patterns to have an annular shape. As illustrated in Fig. 3(a), the source parameters to be optimized include the outer partial coherence factor σ_{out} and the ring width σ_w [47]. Thus, the source \mathbf{J} in Eq. (1) is formulated as

$$\mathbf{J}(x_s, y_s, \sigma_{out}, \sigma_w) = \begin{cases} 1 & \text{if } (\sigma_{out} - \sigma_w) \leq r_s \leq \sigma_{out} \\ 0 & \text{otherwise} \end{cases}, \quad (13)$$

where $\sigma_{out} \in (0, 1]$, $\sigma_w \in (0, \sigma_{out})$, and $r_s = \sqrt{x_s^2 + y_s^2}$ is the distance from the source center to the source point (x_s, y_s) . In order to apply the gradient-based algorithm to optimize the source parameters, we need to approximate the indifferentiable source function in Eq. (13) by a differentiable arched function as following [47]:

$$\mathbf{J}(x_s, y_s, \sigma_{out}, \sigma_w) = \frac{1}{(r_s/\sigma_{out})^{2b_s} + 1} - \frac{1}{[r_s/(\sigma_{out} - \sigma_w)]^{2b_s} + 1}, \quad (14)$$

where b_s is the steepness index of the arched function. Hereafter, we use a common notation σ to represent the parameters σ_{out} or σ_w . Assume $\sigma \in [\sigma_{min}, \sigma_{max}]$, where σ_{min} and σ_{max} are the lower and upper bounds of σ . In order

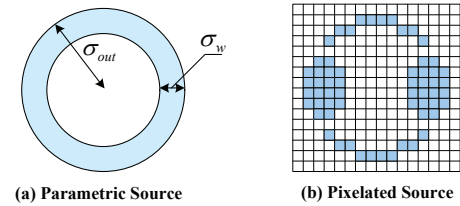


Fig. 3. The (a) parametric source and (b) pixelated source.

to reduce the bound-constrained optimization problem to an unconstrained optimization problem, we adopt the following parametric transformation:

$$\begin{aligned} \sigma &= (\sigma_{max} - \sigma_{min}) \cdot \text{sig}(\Omega_\sigma, 0) + \sigma_{min} \\ &= \frac{\sigma_{max} - \sigma_{min}}{\exp(-b_\sigma \cdot \Omega_\sigma) + 1} + \sigma_{min}, \end{aligned} \quad (15)$$

where b_σ is the steepness index of the sigmoid function, and $\Omega_\sigma \in (-\infty, \infty)$ is the transformed parameter of σ . It is noted that the above parametric source model can be generalized to other kinds of source shapes, such as dipole, quadrupole sources and so on.

On the other hand, the development of pixelated EUV source has currently been enabled by freeform illumination pupils [31]. As illustrated in Fig. 3(b), the pixelated SMO methods grid the source pattern into $N_s \times N_s$ pixels, and the value of each pixel represents the intensity of the corresponding source point. In order to consider the general cases of freeform sources, we assume that the source pixels can be assigned to any real values in the range of $[0, 1]$, and all source pixels can be optimized during the SMO flow. Thus, the source \mathbf{J} in Eq. (1) is formulated as

$$\mathbf{J} = f(\Omega_S) = \frac{1 + \cos \Omega_S}{2}, \quad (16)$$

where Ω_S is an $N_s \times N_s$ real matrix, whose entry values can be changed in the range of $(-\infty, \infty)$.

IV. FORMULATIONS OF PARAMETRIC AND PIXELATED SMO PROBLEMS

A. Formulation of Parametric SMO

The goal of parametric SMO is to search the optimal $\hat{\sigma}_{out}$, $\hat{\sigma}_w$, $\hat{\Theta}_M$ and $\hat{\Theta}_S$ to minimize the cost function D , i.e.

$$(\hat{\sigma}_{out}, \hat{\sigma}_w, \hat{\Theta}_M, \hat{\Theta}_S) = \arg \min_{\sigma_{out}, \sigma_w, \Theta_M, \Theta_S} D, \quad (17)$$

where the cost function is

$$D = F + \sum_{i=1}^m \gamma_i R_i. \quad (18)$$

In Eq. (18), F is the pattern fidelity term that is given by

$$\begin{aligned} F &= \sum_{m=1}^N \sum_{n=1}^N \Pi(m, n) \cdot [\tilde{\mathbf{Z}}(m, n) - \mathbf{Z}(m, n)]^2 \\ &= |\sqrt{\Pi} \odot (\tilde{\mathbf{Z}} - \mathbf{Z})|_2^2, \end{aligned} \quad (19)$$

where $\tilde{\mathbf{Z}} \in \mathbb{R}^{N \times N}$ is the target pattern with all entries equal to 0 or 1, and \mathbf{Z} is the print image described in Eq. (7). Π is a weight matrix to locally emphasize or de-emphasize the image distortion according to whether the underlying region is a critical region or not. In Eq. (18), R_i is any regularization term to bias the solution space to have some expected properties or merits, and γ_i is the weight parameter. As mentioned in Sec. III, we use the sigmoid function to approximate the hard threshold function $\Gamma\{\bullet\}$ in Eq. (11). To suppress the approximation error, this paper adopts the discretization penalty as following

$$R_d = \sum_{m=1}^N \sum_{n=1}^N \left\{ 1 - \frac{1}{[(n_r - n_a)/2]^2} \cdot \left[\mathbf{M}(m, n) - \frac{n_r + n_a}{2} \right]^2 \right\}. \quad (20)$$

In order to apply the conjugate gradient algorithm to solve for the parametric SMO problem, we need to calculate the gradients of cost function with respect to the source and mask variables. Based on the parametric transformation in Eq. (15),

and considering $\partial R_d / \partial \Omega_\sigma = 0$, the derivative of cost function to the source variable Ω_σ is

$$\frac{\partial D}{\partial \Omega_\sigma} = \frac{\partial F}{\partial \Omega_\sigma} + \frac{\partial R_d}{\partial \Omega_\sigma} = \frac{\partial F}{\partial \Omega_\sigma}. \quad (21)$$

The detailed method to calculate the derivative in Eq. (21) is provided in Appendix A.

The gradients of cost function to the mask variables Θ_M and Θ_S are formulated as

$$\nabla D|_{\Theta_M} = \nabla F|_{\Theta_M} + \nabla R_d|_{\Theta_M}, \quad (22)$$

$$\nabla D|_{\Theta_S} = \nabla F|_{\Theta_S} + \nabla R_d|_{\Theta_S}. \quad (23)$$

The detailed methods to calculate the derivatives in Eqs. (22) and (23) are provided in Appendix B.

B. Formulation of Pixelated SMO

Given the binary target pattern $\tilde{\mathbf{Z}}$, the goal of pixelated SMO is to search the optimal matrices $\hat{\mathbf{J}}$, $\hat{\Theta}_M$ and $\hat{\Theta}_S$ to minimize the cost function D , i.e.

$$\begin{aligned} (\hat{\mathbf{J}}, \hat{\Theta}_M, \hat{\Theta}_S) &= \arg \min_{\mathbf{J}, \Theta_M, \Theta_S} D \\ &= \arg \min_{\mathbf{J}, \Theta_M, \Theta_S} (F + \gamma_d R_d + \gamma_S R_S), \end{aligned} \quad (24)$$

where F and R_d are described in Eqs. (19) and (20). R_S is referred to as the source penalty. Since pixelated SMO algorithm may result in freeform source patterns, we need to use the source penalty R_S to increase the minimum integrated pupil fill percentage and minimum dark pixel intensity. Otherwise, the imaging aberration or lens damage may be caused by the lens heating effects. According to [10], the source penalty term is formulated as

$$R_S = - \sum_{x_s} \sum_{y_s} \text{sig}\{\mathbf{J}(x_s, y_s), 0\}, \quad (25)$$

where the function “sig” is the same as Eq. (6) with $a = 25$ and $t_r = 0$. According to the parametric transformation in Eq. (16), the pixelated SMO optimizes the matrix Ω_S instead of \mathbf{J} .

Similar to Sec. IV-A, we need to calculate the gradients of cost function with respect to the source and mask variables. Since $\nabla R_d|_{\Omega_S} = \mathbf{0}$, the gradient of cost function to Ω_S is

$$\nabla D|_{\Omega_S} = \nabla F|_{\Omega_S} + \gamma_S \nabla R_S|_{\Omega_S}. \quad (26)$$

The detailed method to calculate the gradient in Eq. (26) is provided in Appendix C. On the other hand, the gradients of cost function to the mask variables Θ_M and Θ_S are described in Appendix B.

V. GRADIENT-BASED SMO ALGORITHMS FOR EUV LITHOGRAPHY

This section develops gradient-based algorithms to solve for the SMO problems proposed in Sec. IV. Figure 4(a) is the main flowchart of the proposed SMO algorithms. Figures 4(b) and 4(c) show the flowcharts of the two sub-procedures invoked by

the main flow, namely “Method 1” and “Method 2”, respectively. In Figs. 4(b) and 4(c), the notation \mathbf{X} represents the source or mask variables to be optimized. For the parametric SMO, the source variables are $\Omega_{\sigma_{out}}$ and Ω_{σ_w} . For the pixelated SMO, the source variable is Ω_S . The mask variables are always Θ_M and Θ_S . Previously, we developed an efficient and

where

$$T = [\mathbf{W} \otimes \tilde{\mathbf{Z}}](m, n) - \sum_p \sum_q \mathbf{W}(p, q). \quad (28)$$

In Eq. (28), $m, n = 1, 2, \dots, N$, $p, q = 1, 2, \dots, N_M$, and $\tilde{\mathbf{Z}}$ is the target pattern. Based on Eq. (27), the MF of initial mask pattern is represented by the binary matrix $\bar{\mathbf{M}}_M = \Gamma(\mathbf{W}_M \otimes \Theta_M - 1)$. Then, the other mask variable matrix Θ_S is initialized as

$$\Theta_S^0(m, n) = \begin{cases} 1 & \epsilon_T = \epsilon_{seed} \\ 0 & \epsilon_T \neq \epsilon_{seed} \end{cases}, \quad (29)$$

where ϵ_T is the distance between $\Theta_S^0(m, n)$ and $\bar{\mathbf{M}}_M$, and ϵ_{seed} is a parameter to determine the location of the initial SRAFs. For a manufacturable mask, the distance between the MFs and SRAFs cannot be smaller than a predefined threshold ϵ_D , which is defined according to the state of art of mask fabrication. Thus, ϵ_{seed} should satisfy the following constraint

$$\epsilon_{seed} \geq \epsilon_D + pixel_M \cdot \frac{N_S}{2}, \quad (30)$$

where $pixel_M$ is the pixel size on mask side, and N_S is the lateral dimension of the basis block \mathbf{W}_S for the SRAFs. Then, the optimization direction \mathbf{P} in Figs. 4(b) and 4(c) is initialized as $\mathbf{P}^0 = -\nabla D|_{\mathbf{X}^0}$, where D is the cost function, and \mathbf{X}^0 represents the initial variables to be optimized.

After the initialization step, the source is individually optimized by fixing the mask pattern. The individual source optimization stage is used to rapidly reduce the cost function. In each iteration, the source variables are updated by “Method 1” as shown in Fig. 4(b). “Method 1” is a typical conjugate gradient approach, where s is the step length [48]. It is noted that for the source optimization, the **Step 2** in “Method 1” is skipped. The source optimization is terminated whenever the loop number reaches a prescribed upper limit, or the pattern error (PE) is reduced below a tolerable level. The pattern error is defined as

$$\text{Pattern Error} = \|\tilde{\mathbf{Z}} - \mathbf{Z}\|_2^2, \quad (31)$$

where \mathbf{Z} is described in Eq. (5).

After the individual source optimization stage, the simultaneous source and mask optimization is carried out to jointly update the source and mask variables. In each iteration, the source variables are updated using “Method 1” with **Step 2** skipped, and the mask variables Θ_M and Θ_S are updated using “Method 1” or “Method 2”. The details of mask optimization process were described in [5]. But, Ref. [5] focuses on OPC method without source optimization.

Due to the length limit of this paper, we just briefly summarize the method to update mask variables in the following. First, we relax the entry values of Θ_M and Θ_S to the range of [0,1], and update Θ_M using “Method 1”. Then, the binary coefficient matrix $\bar{\Theta}_M$ and its corresponding MF pattern are calculated as

$$\begin{aligned} \bar{\Theta}_M &= \Gamma\{\Theta_M - 0.5\}, \\ \bar{\mathbf{M}}_M &= \Gamma\{\mathbf{W}_M \otimes \bar{\Theta}_M - 1\}. \end{aligned} \quad (32)$$

During the MF update, we only modify the mask shapes but don't change the polygon number included in the MF pattern.

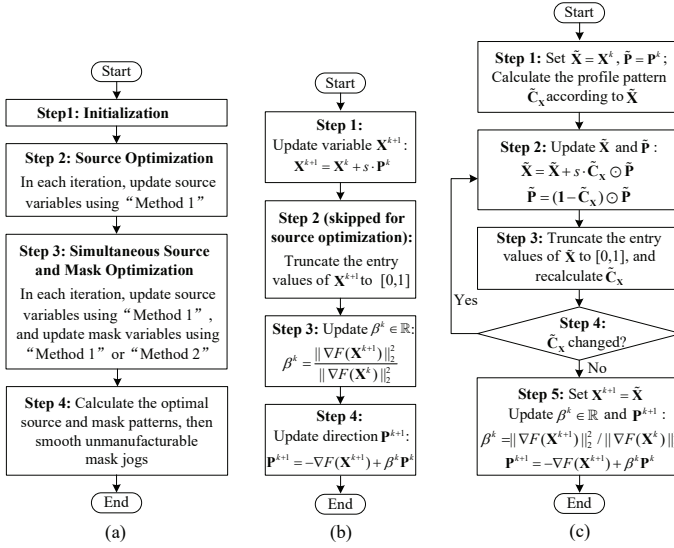


Fig. 4. The flowcharts for the (a) main SMO procedure, (b) “Method 1”, and (c) “Method 2” (Figures 4(b) and 4(c) are modified from Fig. 3 in Ref. [5]).

stable hybrid SMO method in DUV lithography system that outperforms the simultaneous and sequential SMO approaches [10], [22]. In the previous hybrid SMO method, both of the source and mask were represented by pixelated patterns. Thus, the optimized mask pattern may contain complex features that are hard to fabricate. This paper generalizes the hybrid SMO flow into EUV lithography by invoking EUV imaging models and the block-based mask model to improve the mask manufacturability. In each iteration of the optimization algorithm, the locations of the blocks in MFs and SRAFs are updated together to pursue the optimal mask pattern. Note that the block-based OPC algorithm proposed in [35] successively optimizes the MFs and SRAFs, thus apt to converge to a sub-optimal solution. In addition, the proposed hybrid SMO method in this paper can optimize the source patterns in both parametric and pixelated modes.

At the beginning of the algorithms, we initialize the variables and optimization parameters as follows. For the parametric source, we first initialize the outer partial coherence factor $\Omega_{\sigma_{out}}^0$ and the ring width $\Omega_{\sigma_w}^0$. For the pixelated source, the matrix Ω_S is initialized as $\Omega_S^0 = \pi \tilde{\mathbf{J}}/5 + 9\pi(1 - \tilde{\mathbf{J}})/10$, where $\tilde{\mathbf{J}} \in \mathbb{R}^{N_S \times N_S}$ represents the initial source pattern with all entries equal to 0 or 1. The one-valued and zero-valued pixels in $\tilde{\mathbf{J}}$ correspond to the bright and dark source points, respectively. The mask variable matrix Θ_M is initialized as

$$\Theta_M^0(m, n) = \begin{cases} 0.9 / \sum_p \sum_q \mathbf{W}(p, q) & \text{if } T < 0 \\ 1 & \text{if } T = 0 \end{cases}, \quad (27)$$

Thus, if the polygon number in MF is changed, we will restore Θ_M to its value in the last iteration, and then re-update it using “Method 2”. According to Fig. 4(c), “Method 2” only updates the entries of Θ_M along the boundaries of MF pattern, thus keeping the polygon number of MF invariant. After Θ_M is updated, we update Θ_S using “Method 1” to insert additional SRAFs around MFs. To preserve the mask manufacturability, the minimum distance between MFs and SRAFs must be larger than or equal to a predefined threshold [35]. To satisfy this manufacturing constraint, we need to turnoff any entry of Θ_S that induces the SRAF too close to the MF. Hence, after the Θ_S is updated, we need to modify it as

$$\Theta_S(m, n) = \begin{cases} \Theta_S(m, n) & \epsilon_T > (\epsilon_D + pixel_M \cdot \frac{N_S}{2}) \\ 0 & \text{otherwise} \end{cases}, \quad (33)$$

where ϵ_T is the distance between $\Theta_S(m, n)$ and \mathbf{M}_M , ϵ_D is the allowable minimum distance between MFs and SRAFs, $pixel_M$ is the pixel size on mask plane, and N_S is the lateral size of the basis block \mathbf{W}_S . Whenever the maximum loop number is reached, or the PE is reduced below a tolerable level, the simultaneous SMO procedure will be terminated.

In the final step of hybrid SMO flow, we calculate the optimal source and binary mask patterns from the optimized variables. In order to further improve the mask manufacturability, the unmanufacturable jogs on the mask pattern are smoothed using the method proposed in [35].

As mentioned above, the mask shadowing effect has pronounced influence on the EUV lithography imaging performance. In the following, we use a retargeting method concatenated to the gradient-based SMO algorithms, which provides a first approach to compensate for the mask shadowing effect based on the calibrated model. Since the mask shadowing effect will shrink the print image by a width of B , we could inversely compensate for the shadowing effect by adding bias on the target layout before source and mask optimization. The principle of the retargeting method is shown in Fig. 2. Given the target layout in Fig. 2(a), we first calculate the shadowing width B on the layout contour according to Eqs. (9) and (10). Then, we dilate the boundary of the target layout by width B . The dilated target layout is shown by the black solid box in Fig. 2(b). It is noted that the biases imposed on the near side and far side of the layout pattern are different. Then, we use the dilated layout as the target layout to optimize the source and mask. Without the mask shadowing effect, the SMO algorithm will lead to a print image close to the dilated target layout. However, the shadowing effect will shrink the print image as the blue dashed line in Fig. 2(b), which is approximate to the original target layout in Fig. 2(a). Based on this idea, we could pre-compensate the mask shadowing effect by retargeting the desired pattern, and the print image obtained by the SMO algorithms will automatically follow the original target layout. The mask shadowing model in [6] is an approximate calibration model. However, other more rigorous models can be applied to the proposed retargeting method to improve the compensation accuracy for the mask shadowing effect.

This section proposes a general model-based EUV SMO

framework, where the modified conjugate gradient algorithm is chosen as an example to iteratively optimize the source and mask patterns. However, the conjugate gradient algorithm may not be efficient enough to solve for large-scale optimization in the real applications. The computational efficiency of the proposed methods can be improved by applying other numerical algorithms [31], or advanced signal processing techniques, such as the compressive sensing [49], [50], sequential signal estimation [51], machine learning [52] and so on.

VI. SIMULATIONS AND ANALYSIS

This section provides simulations of the proposed SMO methods and compares different SMO algorithms using the test layouts with 22nm and 16nm critical dimensions. In the following, we evaluate and compare different SMO algorithms from the aspects of image fidelity, convergence property, runtime and mask manufacturability. We use the PE, edge placement error (EPE) and normalized image log slope (NILS) as the criterions to evaluate the image performance. The PE is defined in Eq. (31). The EPE indicates the error of the actual printed edge position with respect to the target. In this paper, the EPE is defined as the average value of EPEs along the entire layout contour except for the corners, such that

$$EPE = \frac{1}{L_c} \left\{ \oint_c EPE(s) ds \right\}, \quad (34)$$

where c indicates the layout contour along all boundaries except for the corners, ds is the infinitesimal along c , and L_c is the overall length of c . NILS measures the slope of aerial image normalized by CD at the printed contour. The definition of NILS is as following:

$$NILS = \frac{CD}{\mathbf{I}_{con}} \times \frac{d\mathbf{I}}{dx} \bigg|_{\mathbf{I}_{con}}, \quad (35)$$

where \mathbf{I}_{con} is the intensity of aerial image on the contour, and $d\mathbf{I}/dx$ is the derivative of aerial image along the direction perpendicular to the contour.

All of the following simulations are implemented using Matlab on a computer with Intel(R) Xeon(R) E5-2650 CPU, 2.60GHz, and 63.00GB of RAM. The runtime is calculated by Matlab. In addition, we adopt the trapezoid counts (#Trapezoid) in the fractured masks to evaluate the mask manufacturability [53], [35]. Given a mask pattern, we first fracture it into a set of overlapped or non-overlapped trapezoids. Less trapezoid count means the lower mask complexity and preferable manufacturability.

A. Simulations and Analysis using Test Layout with 22nm Critical Dimension

Figure 5 illustrates the simulations using test layout with $CD = 22\text{nm}$. In this simulation, the SMO algorithms are used to compensate the OPE, flare, and photoresist effects, but the mask shadowing effect is not considered. From left to right, it shows the source patterns, mask patterns, and the corresponding print images, respectively. From top to bottom, it shows the simulation results of the initial case, OPC, parametric SISMO, parametric HSMO, pixelated SISMO and pixelated

HSMO, respectively. In these simulations, the wavelength of light source is $\lambda = 13.5\text{nm}$. The numerical aperture (NA) of the EUV lithography system is 0.25, and the demagnification factor is $R_M = 4$. The lateral sizes of source and mask patterns are $N_s = 41$ and $N = 201$, respectively. For the source patterns, the colors toned from black to white represent the light intensity from 0 to 1. For the mask patterns, the multilayer covers the complete mask substrate, and the absorbers cover a part of the multilayer. The black and white areas on the mask represent the absorbers and the uncovered multilayer regions, respectively. In the following simulations, the overall iteration numbers of OPC and SMO algorithms are all 150.

Figure 5(a) is the initial source pattern, which is an unpolarized annular illumination. The outer partial coherence factor is $\sigma_{out} = 0.84$, and the ring width is $\sigma_{width} = 0.6$. Figure 5(b) is the initial mask, which has the same geometries as the target pattern. The pixel size on the mask is $pixel_M = 11\text{nm}$, and the pixel size on the wafer is $pixel_W = 2.75\text{nm}$. Figure 5(c) illustrates the print image if the initial source and mask are used.

Figure 5(d) is the source used in OPC algorithm, which is the same as the initial source. Figure 5(e) shows the optimized mask pattern using OPC algorithm after smoothing the unmanufacturable jogs. Figure 5(f) shows the print image of the OPC algorithm. In OPC algorithm, the step lengths to update Θ_M and Θ_S are set as $s_{\Theta_M} = s_{\Theta_S} = 0.1$. The weight of mask discretization penalty in Eq. (20) is $\gamma_d = 0.0005$. In Eqs. (2)-(4), we assign $TIS = 16.9\%$, $n_f = 1.15$, $r_{min} = 200\text{nm}$, and $\sigma_p = 18/(2\sqrt{2}\ln 2)$. In Eq. (11), the energy reflectivities of the multilayers and absorbers are set to be 64% and 0.5%, thus $n_r = \sqrt{64\%}$ and $n_a = \sqrt{0.5\%}$. These parameters are adopted from Refs. [38] and [4]. In practice, the reflectivity and phase of the reflected EUV light may vary with the illumination direction. For simplicity, this paper assumes the constant reflectivity, and represents the mask shadowing effect by the calibrated model mentioned above. In Eq. (6), we assign $a = 25$, and $t_r = 0.25$. In Eq. (19), $\Pi(m, n) = 1.6$ within the band between the target boundaries and the extended target contour with 9 pixels away from original boundaries, and $\Pi(m, n) = 1$ in other areas. The lateral sizes of \mathbf{W}_M and \mathbf{W}_S are set as $N_M = 5$ and $N_S = 3$, respectively. In Eqs. (29) and (30), $\epsilon_{seed} = 27 \cdot pixel_M$, and $\epsilon_D = 19 \cdot pixel_M$. In practical applications, these parameters above should be adjusted according to the specific lithography tool, process, experimental data and manufacturing constraints on the product line. However, our proposed SMO frameworks are suitable for different parameters. Note that the target pattern is symmetric along the horizontal midline. For simplicity, the two-fold symmetry of the mask along the horizontal midline is imposed during the optimization procedure. Specifically, we first update the pixels on the top half mask, and then update the symmetric pixels on the bottom half in the same way. It is noted that the oblique light incidence and three-dimensional EUV mask structure usually lead to asymmetric optimal source and mask patterns. As described in Sec. VI-C, the proposed algorithms can be easily extended to support the asymmetric optimization of source and mask.

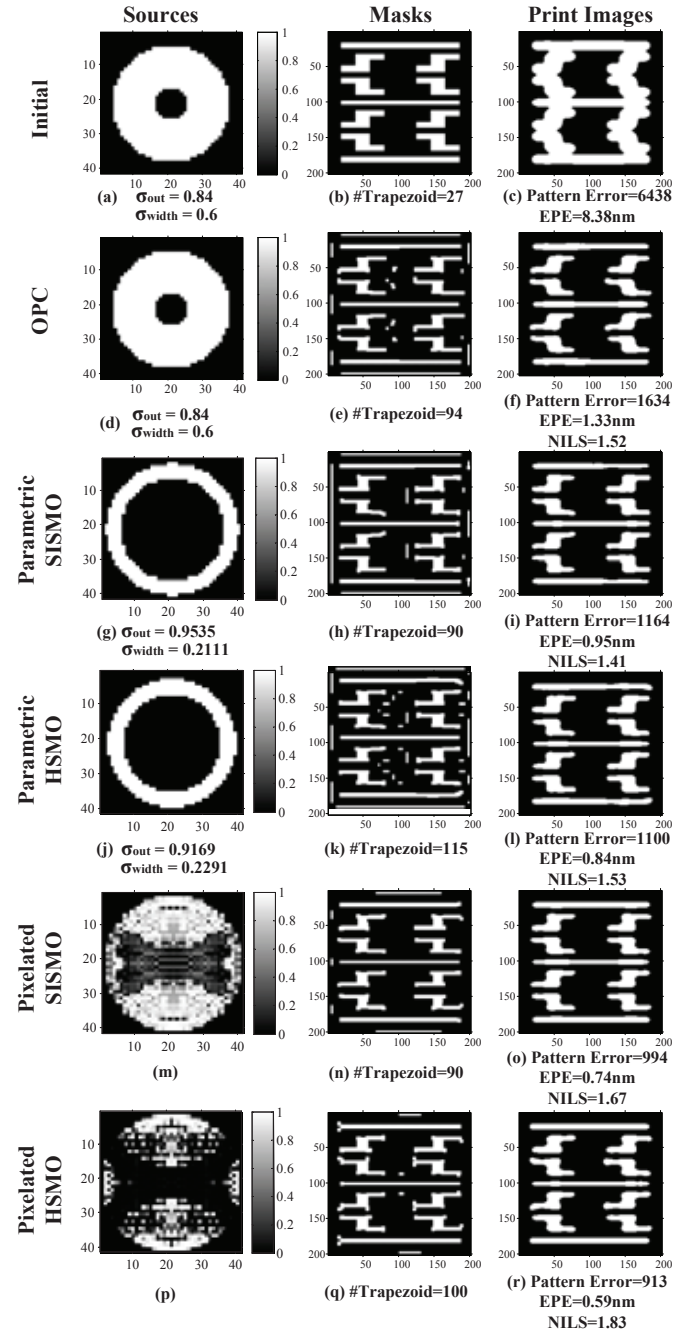


Fig. 5. Simulations of the OPC and different SMO methods using the test layout with 22nm critical dimension.

The third row in Fig. 5 shows the simulation results of parametric SISMO method. In Eqs. (14) and (15), $b_s = 40$ and $b_\sigma = 0.05$. The step lengths to update $\Omega_{\sigma_{out}}$ and $\Omega_{\sigma_{width}}$ are $s_{\Omega_{\sigma_{out}}} = s_{\Omega_{\sigma_{width}}} = 0.01$. In Eq. (14), we use a differentiable arched function to approximate the parametric source pattern. Thus, at the end of the parametric SMO algorithm, we need to threshold the source pattern by 0.5, resulting in a binary source. Other parameters of the parametric SMO algorithm are the same as the OPC simulation in the second row. The optimized source variables obtained by the parametric SISMO method are $\hat{\sigma}_{out} = 0.9535$ and $\hat{\sigma}_{width} = 0.2111$.

The fourth row in Fig. 5 shows the simulation results of parametric HSMO method. The HSMO flow consists of 10 times individual source optimization followed by 140 times SISMO. In the individual source optimization, the step lengths are set to be $s_{\Omega_{out}} = s_{\Omega_{width}} = 0.1$. In the SISMO procedure, the source step lengths are $s_{\Omega_{out}} = s_{\Omega_{width}} = 0.01$. Other parameters are the same as the OPC simulation. The optimized source variables obtained by the parametric HSMO method are $\hat{\sigma}_{out} = 0.9169$ and $\hat{\sigma}_{width} = 0.2291$.

The fifth row in Fig. 5 shows the simulation results of pixelated SISMO method. The step length to update the source variable is $s_{\Omega_S} = 0.005$, and the weight of source penalty is $\gamma_S = 0.0001$. Other parameters are the same as the OPC simulation. In the optimization process, the fourfold symmetry is imposed on the source pattern. In particular, we first update the source pixels of the top left quarter, then update the symmetric pixels of the other three quarters in the same way. It is straightforward to generalize the proposed algorithm to take into account the asymmetric source optimization. When the SISMO algorithm is terminated, we shut down all source pixels with intensities lower than a threshold $t_S = 0.1$ to reduce the source complexity.

The sixth row in Fig. 5 shows the simulation results of pixelated HSMO method. The HSMO flow consists of 2 times individual source optimization and 148 times SISMO. In the individual source optimization, the step length is $s_{\Omega_S} = 0.5$, and the weight of source penalty is $\gamma_S = 0.001$. In the SISMO procedure, the source step length is $s_{\Omega_S} = 0.03$, and the weight of source penalty is $\gamma_S = 0.001$. Other parameters are the same as the OPC simulation.

The top half of Table I lists the PEs, EPEs, NILSs, trapezoid counts and runtimes of the simulations mentioned above. The measurement positions of the NILSs are marked in Fig. 6. The average NILS on positions ①, ②, ③, and ④ is used to evaluate the slope of the aerial image. From these simulation data, we can compare the OPC and different SMO algorithms. In general, the image fidelity rank from the best to the worst is pixelated HSMO, pixelated SISMO, parametric HSMO, parametric SISMO, and OPC. The parametric SISMO and parametric HSMO methods jointly optimize the source and mask, thus achieving much lower PEs and EPEs than the OPC method. On the other hand, the pixelated source model introduces much higher degree of optimization freedom than the parametric source model, thus the pixelated SISMO and pixelated HSMO methods can further reduce the PE and EPE values, and improve the NILS of the aerial image. However, the pixelated SMO methods dramatically increase the variable dimensions, and take much longer runtimes than the parametric SMO methods. It is noted that most of the SMO algorithms lead to higher NILS than the OPC algorithm, except for the parametric SISMO algorithm. That is because the NILS is not directly included in the cost function, thus the parametric SISMO cannot guarantee the increment of NILS during the optimization procedure. It is also shown that the pixelated SISMO and HSMO methods lead to the same or less trapezoid counts than the parametric SISMO and HSMO methods, respectively. That means the pixelated SMO is more beneficial to improve the mask manufacturability. The reason is the

pixelated SMO increases the source optimization freedom and share the pressure with mask optimization. Thus, in contrast to the parametric SMO, the pixelated SMO can achieve better imaging performance and simpler mask patterns.

TABLE I
THE PEs, EPEs, NILSs, RUNTIMES AND TRAPEZOID COUNTS OF OPC AND DIFFERENT SMO METHODS, WHERE “#TRAP” MEANS “#TRAPEZOID”.

CD	Method	PE	EPE (nm)	NILS	#Trap	Runtime (s)
CD=22nm	Initial	6438	8.38	–	27	–
	OPC	1634	1.33	1.52	94	8388
	Parametric SISMO	1164	0.95	1.41	90	9122
	Parametric HSMO	1100	0.84	1.53	115	5743
	Pixelated SISMO	994	0.74	1.67	90	33615
	Pixelated HSMO	913	0.59	1.83	100	18926
CD=16nm	Initial	6812	6.28	–	27	–
	OPC	1859	1.64	1.06	122	9254
	Parametric SISMO	1543	1.23	1.36	118	9169
	Parametric HSMO	1252	1.04	1.37	126	8627
	Pixelated SISMO	1411	1.21	1.72	91	22952
	Pixelated HSMO	1162	0.85	1.66	121	17447

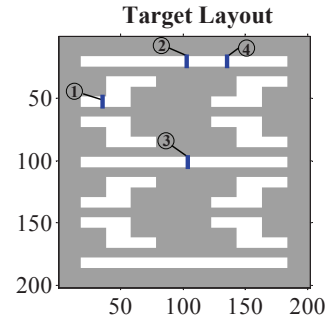


Fig. 6. Measurement positions of the process windows.

Next, We make comparison between the simultaneous and hybrid SMO algorithms. It is observed that the parametric and pixelated HSMO algorithms outperform the SISMO algorithms in both of the imaging performance and computational efficiency. That is because the HSMO algorithms take advantages of both individual source optimization and SISMO algorithms. At the beginning, the individual source optimization is operated to rapidly reduce the cost function. Subsequently, the SISMO step is carried out to exploit the synergy between source optimization and mask optimization. The hybrid optimization flow is more flexible than the SISMO flow to control the optimization process, and results in higher image fidelity. In addition, the individual source optimization step in HSMO algorithms does not need to calculate the

gradient of cost function to the mask variables. This will further reduce the computational complexity of HSMO methods. However, the parametric and pixelated HSMO algorithms lead to larger trapezoid counts and more complex masks than the corresponding SISMO algorithms, respectively. This can be explained as follows. Given the source model, the HSMO and SISMO methods have the same source variable dimension. In order to achieve better image fidelity, HSMO has to optimize the mask more aggressively than the SISMO to further reduce the image distortion.

Figure 7(a) illustrates the convergence curves of cost functions for the OPC and different SMO methods. The X-axis and Y-axis represent the iteration numbers and the values of cost functions, respectively. The convergence of parametric SMO methods is more stable than the pixelated SMO methods. That is because the pixelated SMO may optionally change the freeform source pattern, while the parametric SMO can only optimize two source variables. Thus, the parametric SMO methods pose more constraints on the optimization procedure and suppress the oscillations of convergence curves. Another finding is that the pixelated HSMO converges more steadily than the pixelated SISMO. The reason is that the pixelated HSMO starts with a few iterations of individual source optimization to rapidly achieve a lower pattern error level. Subsequently, the pixelated HSMO gradually modifies the source and mask together. However, the pixelated SISMO intensively co-optimizes the source and mask all the way. Therefore, after the first several iterations, the pixelated HSMO converges more smooth than the pixelated SISMO.

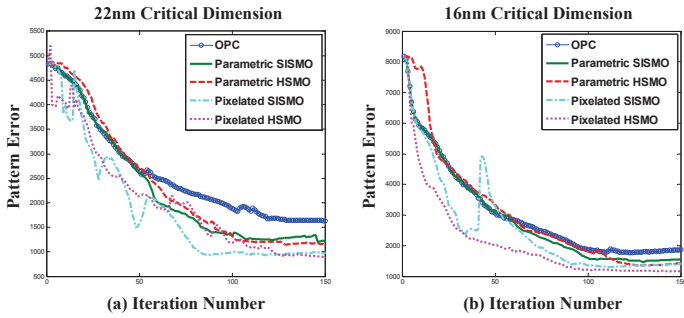


Fig. 7. Convergence curves of cost functions for OPC and different SMO methods with (a) 22nm critical dimension and (b) 16nm critical dimension.

Process variations always exist in practical EUV lithography systems. Process window is extensively used to assess the robustness of lithography system to process variations. Figure 8(a) compares the overlapped process windows obtained by OPC and different SMO methods with a 22nm layout pattern. The X and Y axes of the process window represent the depth of focus (DOF) and exposure latitude (EL), respectively. Larger process window means that the lithography system can get a desired imaging performance with larger tolerance of defocus and dose variation. For the target layout in Fig. 6, we first individually calculate the process windows at the locations ①, ②, ③, and ④. Then, the overlapped area among these process windows is plotted in Fig. 8(a). It is observed that all of the SMO algorithms obtain larger process windows than

the OPC algorithm, and the HSMO methods outperform the SISMO methods in process windows.

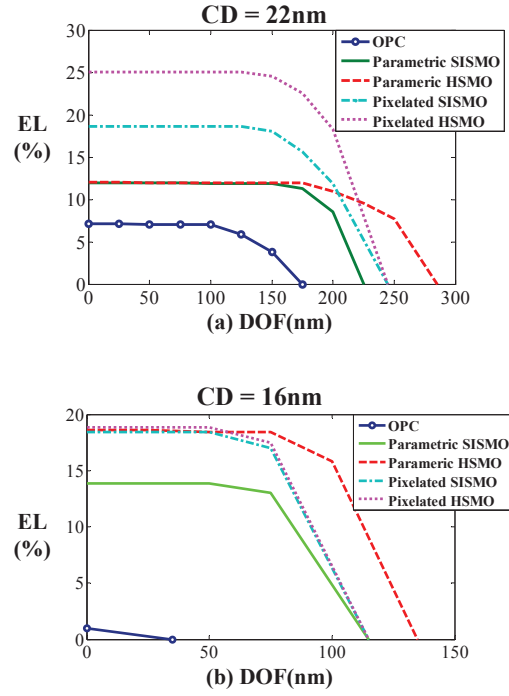


Fig. 8. Process windows obtained by OPC and different SMO methods with (a) 22nm critical dimension and (b) 16nm critical dimension.

B. Simulations and Analysis using Test Layout with 16nm Critical Dimension

Figure 9 illustrates the simulation results using test layout with CD=16nm. In this simulation, the SMO algorithms are used to compensate the OPE, flare, and photoresist effects, but the mask shadowing effect is not considered. The NA of EUV lithography system is 0.33. The overall iteration numbers of OPC and SMO algorithms are all 150. The initial source in Fig. 9(a) is the same as Fig. 5(a). On the mask side, the pixel size is $pixel_M = 8\text{nm}$. On the wafer side, the pixel size is $pixel_W = 2\text{nm}$. The second row in Fig. 9 illustrates the simulation results of OPC method, where we set $\epsilon_D = 15 \cdot pixel_M$ and $\epsilon_{seed} = 20 \cdot pixel_M$ in Eqs. (29) and (30). Other parameters are the same as those used in Fig. 5. Hereafter, if not mentioned, the parameter settings are the same as the OPC simulation in Fig. 5. For the parametric SISMO, the step lengths are set as $s_{\Omega_{\sigma_{out}}} = s_{\Omega_{\sigma_{width}}} = 0.0002$. The optimized source variables obtained by the parametric SISMO method are $\hat{\sigma}_{out} = 0.8755$ and $\hat{\sigma}_{width} = 0.5383$. For the parametric HSMO, we first run 10 times individual source optimization with the step lengths of $s_{\Omega_{\sigma_{out}}} = s_{\Omega_{\sigma_{width}}} = 0.06$. Then, we run 140 times SISMO with the source step lengths of $s_{\Omega_{\sigma_{out}}} = s_{\Omega_{\sigma_{width}}} = 0.0002$. The optimized source variables are $\hat{\sigma}_{out} = 0.9320$ and $\hat{\sigma}_{width} = 0.4580$. For the pixelated SISMO, we set $s_{\Omega} = 0.0005$ and $\gamma_s = 0.001$. For the pixelated HSMO, we first run 4 times individual source optimization with step length of $s_{\Omega} = 0.01$, and the weight of source penalty is $\gamma_s = 0.002$. Then, we run 146 times SISMO where the source

step length is $s_\Omega = 0.0005$ and the weight of source penalty is $\gamma_s = 0.001$.

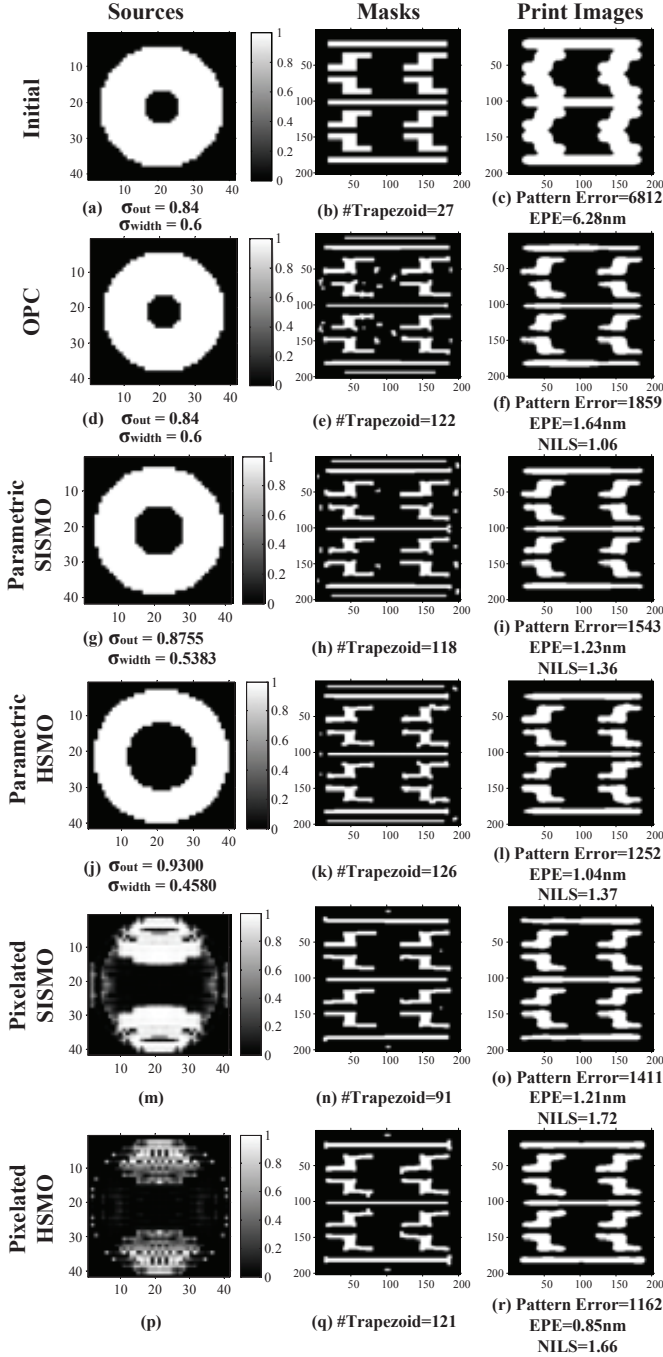


Fig. 9. Simulations of the OPC and different SMO methods using the test layout with 16nm critical dimension.

The PEs, EPEs, NILSs, trapezoid counts and runtimes of the 16nm simulations are listed in the bottom half of Table I. The convergence curves of cost functions are illustrated in Fig. 7(b). A jump is observed in the convergence curve of pixelated SISMO method. That is because the gradient-based algorithm tries to escape from the local minimum and continue to reduce the cost function. Figure 8(b) compares the overlapped process windows obtained by OPC and different SMO

methods with 16nm layout pattern. From these simulation results, we can get the similar conclusions to those from simulations in Fig. 5. One counterexample is that the pixelated SISMO results in higher PE and EPE than the parametric HSMO in 16nm simulations. However, in 22nm simulations the pixelated SISMO results in lower PE and EPE than the parametric HSMO. This indicates that the HSMO is more powerful than SISMO to achieve finer resolvable patterns. So, when the feature size is not so critical, the pixelated SISMO outperforms parametric HSMO due to its abundance of optimization freedom. On the other hand, when the feature size shrinks, the parametric HSMO wins due to its advanced optimization strategy.

In summary, we have provided comprehensive comparison and analysis among different SMO approaches in the aspects of imaging performance, manufacturability, and computational complexity. However, the choice of different SMO algorithms depends on the particular conditions or requirements in the real applications. If the complexity of source pattern is a main concern, the parametric HSMO algorithm is suggested. If the mask manufacturability is the key factor to be addressed, SISMO algorithms are good choices. Otherwise, pixelated HSMO algorithm is recommended, since it achieves superior imaging performance and computational efficiency over other algorithms.

At the end of this section, we propose a penalty method to further improve the NILS of the lithography image. In the cost function of Eq. (18), we add another penalty term R_W , such that the cost function becomes

$$D = F + \gamma_d R_d + \gamma_s R_s + \gamma_w R_w, \quad (36)$$

where

$$R_w = |\sqrt{\Pi} \odot (\alpha_w \tilde{\mathbf{Z}} - \mathbf{I})|_2^2, \quad (37)$$

and α_w is a constant to modify the amplitude of target pattern. The penalty in Eq. (37) enforces the aerial image close to the target layout, so as to improve the slope angle of the aerial image. Figure 10 illustrates the simulation results of the pixelated HSMO algorithm aided by the proposed penalty in Eq. (37), where $\alpha_w = 1.1$ and $\gamma_w = 0.0005$. The top row and bottom row in Fig. 10 show the simulation results using the layouts with 22nm and 16nm critical dimensions, respectively. Comparing to Figs. 5(r) and 9(r), the proposed penalty method can improve the NILS of the lithography systems, while achieve comparable pattern error and EPE on average.

C. Simulations to Compensate for the Mask Shadowing Effect

The mask shadowing effect is not considered in the previous simulations. This section provides the simulations to compensate for the mask shadowing effect using the retargeting method described in Sec. V. In the following simulations, we assume the mask pattern is placed along the X-axis, and the ring slit of exposure field lies in the vertical direction. As shown in Fig. 11, suppose the left side of the layout pattern is the near side with respect to the incident light rays, while the right side of the layout pattern is in the far side. The near side and far side are represented by the red and green lines,

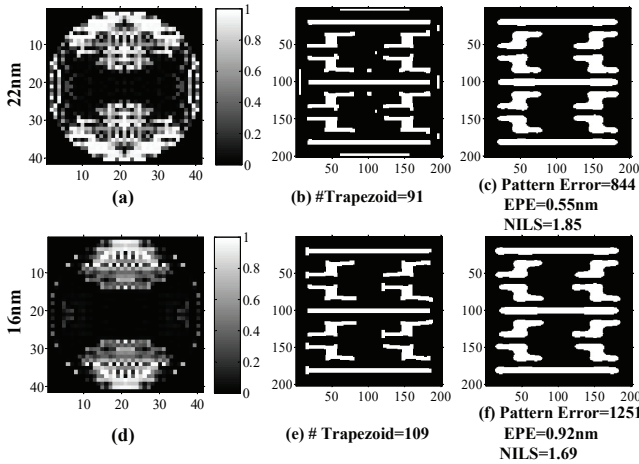


Fig. 10. Simulation results of pixelated HSMO algorithm adied by the penalty term to improve the NILS.

respectively. In order to offset the mask shadowing effect, we can extend the vertical edges of target pattern on the near side by B_n , and extend the vertical edges on the far side by B_f . The values of B_n and B_f can be calculated by Eq. (10) with calibrated parameters. In practice, the values of B_n and B_f depend on the source geometry and the multilayer stack of the mask. Due to cost limitations, calibrating the parameters based on the rigorous simulators or experimental data is not possible. In order to illustrate the feasibility of the retargeting method, we simply assume B_n is equal to one pixel, and B_f is equal to two pixels in the following simulations. It is noted that the proposed algorithms can apply to other values of B_n and B_f .

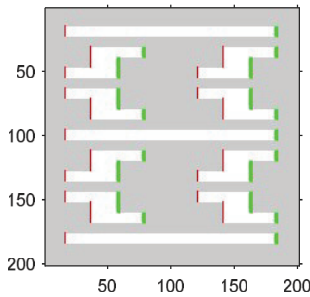


Fig. 11. The retargeting layout pattern, where the red and green lines indicate the locations of the extended edges on the near side and far side, respectively.

The simulation of the retargeting method with CD=22nm are shown in Fig. 12. Figures 12(a) and 12(b) are results of the pixelated HSMO algorithm without considering the mask shadowing effect, which are the same as the source and mask patterns in Figs. 5(p) and 5(q). Figure 12(c) is the corresponding print image by taking into account the mask shadowing effect. Note that Fig. 5(r) is the print image without considering the mask shadowing effect. Comparing Figs. 5(r) and 12(c), the mask shadowing effect will shrink the print image and increase the pattern error. Figures 12(d) and 12(e) are the optimized source and mask patterns by using the retargeting method, which dilates the target layout before

optimization. Figure 12(f) is the corresponding print image. In order to show the capability of our algorithms to support the asymmetric optimization, we relax the symmetric constraints on the source and mask patterns in this simulation. That means we allow the asymmetry of source and mask patterns during the optimization process. It is observed that the retargeting method can reduce the pattern error and EPE based on the calibrated mask shadowing model mentioned above.

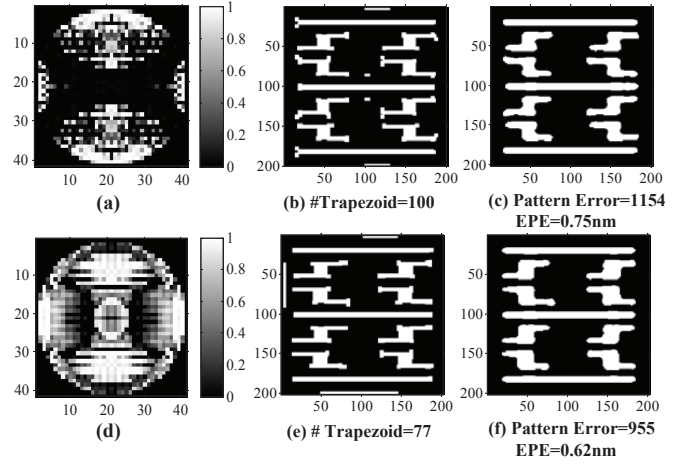


Fig. 12. Simulations with the mask shadowing effect based on 22nm layout pattern. Top row shows the optimized (a) source and (b) mask without considering the mask shadowing effect, and (c) the corresponding print image. The bottom row shows the optimized (a) source and (b) mask using the retargeting method, and (c) the corresponding print image.

Figure 13 illustrates the simulations with mask shadowing effect using 16nm layout pattern. It is shown that the SMO algorithm with retargeting method can effectively reduce the pattern error and EPE based on the approximate EUV lithography imaging models and calibrated mask shadowing model.

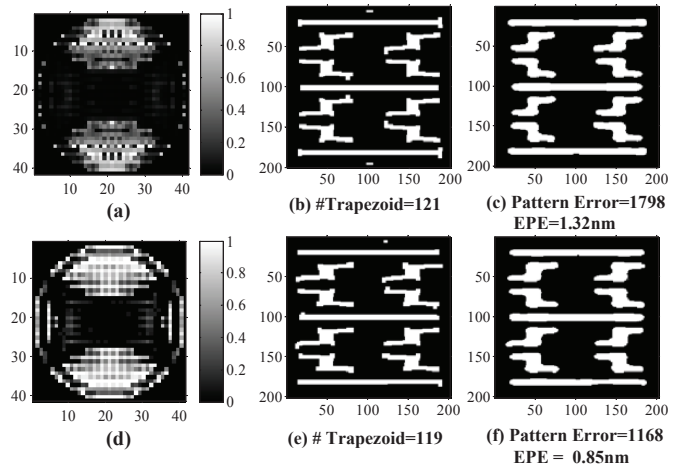


Fig. 13. Simulations with the mask shadowing effect based on 16nm layout pattern. Top row shows the optimized (a) source and (b) mask without considering the mask shadowing effect, and (c) the corresponding print image. The bottom row shows the optimized (a) source and (b) mask using the retargeting method, and (c) the corresponding print image.

VII. CONCLUSION

This paper formulates the SMO problem as an inverse imaging problem based on a coarsely approximate nonlinear model of EUV lithography. A set of gradient-based numerical algorithms are then developed to pursue the optimal source and mask solutions and improve the image performance of EUV lithography systems. In conjunction with the parametric and pixelated source models, the block-based mask model is used to reduce the mask complexity. The traditional and modified conjugate gradient algorithms are used to iteratively optimize the source and mask variables. In addition, the retargeting method is used to pre-warp the target layout to coarsely compensate for the mask shadowing effect. Based on the simulations of 22nm and 16nm layouts, we evaluate and compare different SMO algorithms in the aspects of image performance, convergence property, runtime and mask complexity. It is shown that the parametric SMO methods lead to shorter runtime and manufacture-friendly source patterns with conventional illumination shapes. The pixelated SMO methods can further improve the image fidelity by increasing the degrees of optimization freedom. On the other hand, the HSMO approaches outperform the SISMO approaches in image fidelity and computational efficiency at the cost of increasing the mask complexity. Future work includes the generalization and adaptation of the methods presented in this manuscript to more accurate EUV lithographic models.

APPENDIX A

$$\begin{aligned}
\frac{\partial D}{\partial \Omega_\sigma} &= \frac{\partial F}{\partial \Omega_\sigma} + \frac{\partial R_d}{\partial \Omega_\sigma} = \frac{\partial F}{\partial \Omega_\sigma} \\
&= \sum_{m=1}^N \sum_{n=1}^N \frac{\partial F}{\partial \mathbf{I}_r(m, n)} \cdot \frac{\partial \mathbf{I}_r(m, n)}{\partial \Omega_\sigma} \\
&= - \sum_{m=1}^N \sum_{n=1}^N 2\Pi(m, n) \cdot \left(\tilde{\mathbf{Z}}(m, n) \right. \\
&\quad \left. - \frac{1}{1 + \exp\{-a[\mathbf{I}_r(m, n) - t_r]\}} \right) \\
&\quad \cdot \frac{a \cdot \exp\{-a[\mathbf{I}_r(m, n) - t_r]\}}{(\exp\{-a[\mathbf{I}_r(m, n) - t_r] + 1\})^2} \cdot \frac{\partial \mathbf{I}_r(m, n)}{\partial \Omega_\sigma} \\
&= -a \cdot \sum_{m=1}^N \sum_{n=1}^N 2\Pi(m, n) \cdot [\tilde{\mathbf{Z}}(m, n) - \mathbf{Z}(m, n)] \\
&\quad \cdot \mathbf{Z}(m, n) \cdot [1 - \mathbf{Z}(m, n)] \cdot \frac{\partial \mathbf{I}_r(m, n)}{\partial \Omega_\sigma}. \quad (38)
\end{aligned}$$

In the above equation, the derivative of $\mathbf{I}_r(m, n)$ to Ω_σ is

$$\begin{aligned}
\frac{\partial \mathbf{I}_r(m, n)}{\partial \Omega_\sigma} &= \frac{1}{J_{sum}^2} \left[\frac{\partial \mathbf{I}'_r(m, n)}{\partial \Omega_\sigma} \cdot J_{sum} \right. \\
&\quad \left. - \frac{\partial J_{sum}}{\partial \Omega_\sigma} \cdot \mathbf{I}'_r(m, n) \right], \quad (39)
\end{aligned}$$

where $\mathbf{I}'_r = \sum_{x_s} \sum_{y_s} \{ \mathbf{J}(x_s, y_s) \cdot [\mathbf{H}_r \otimes |\mathbf{H}^{x_s y_s} \otimes (\mathbf{B}^{x_s y_s} \odot \mathbf{M})|^2] \}$. Thus, in Eq. (39),

$$\begin{aligned}
\frac{\partial \mathbf{I}'_r(m, n)}{\partial \Omega_\sigma} &= \sum_{x_s} \sum_{y_s} \left\{ \frac{\partial \mathbf{J}(x_s, y_s)}{\partial \Omega_\sigma} \cdot [\mathbf{H}_r \right. \\
&\quad \left. \otimes |\mathbf{H}^{x_s y_s} \otimes (\mathbf{B}^{x_s y_s} \odot \mathbf{M})|^2] \right\}. \quad (40)
\end{aligned}$$

In order to calculate Eq. (40), we need to first calculate the derivatives of $\mathbf{J}(x_s, y_s)$ to $\Omega_{\sigma_{out}}$ and Ω_{σ_w} , where $\Omega_{\sigma_{out}}$ and Ω_{σ_w} are the transformed parameters of σ_{out} and σ_w , respectively. The derivative of $\mathbf{J}(x_s, y_s)$ to $\Omega_{\sigma_{out}}$ is given by

$$\begin{aligned}
\frac{\partial \mathbf{J}(x_s, y_s)}{\partial \Omega_{\sigma_{out}}} &= \frac{\partial \mathbf{J}(x_s, y_s)}{\partial \sigma_{out}} \cdot \frac{\partial \sigma_{out}}{\partial \Omega_{\sigma_{out}}} \\
&= \left(\frac{2b_s \cdot (r_s / \sigma_{out})^{2b_s-1}}{[(r_s / \sigma_{out})^{2b_s} + 1]^2} \cdot \frac{r_s}{\sigma_{out}^2} \right. \\
&\quad \left. - \frac{2b_s \cdot [r_s / (\sigma_{out} - \sigma_w)]^{2b_s-1}}{\{[r_s / (\sigma_{out} - \sigma_w)]^{2b_s} + 1\}^2} \right. \\
&\quad \left. \cdot \frac{r_s}{(\sigma_{out} - \sigma_w)^2} \right) \cdot \frac{\partial \sigma_{out}}{\partial \Omega_{\sigma_{out}}}. \quad (41)
\end{aligned}$$

On the other hand, the derivative of $\mathbf{J}(x_s, y_s)$ to Ω_{σ_w} is given by

$$\begin{aligned}
\frac{\partial \mathbf{J}(x_s, y_s)}{\partial \Omega_{\sigma_w}} &= \left(\frac{2b_s \cdot [r_s / (\sigma_{out} - \sigma_w)]^{2b_s-1}}{\{[r_s / (\sigma_{out} - \sigma_w)]^{2b_s} + 1\}^2} \right. \\
&\quad \left. \cdot \frac{r_s}{(\sigma_{out} - \sigma_w)^2} \right) \cdot \frac{\partial \sigma_w}{\partial \Omega_{\sigma_w}}. \quad (42)
\end{aligned}$$

According to Eq. (15), both $\partial \sigma_{out} / \partial \Omega_{\sigma_{out}}$ in Eq. (41) and $\partial \sigma_w / \partial \Omega_{\sigma_w}$ in Eq. (42) can be written in the form of

$$\frac{\partial \sigma}{\partial \Omega_\sigma} = \frac{b_\sigma \cdot (\sigma_{max} - \sigma_{min}) \cdot \exp(-b_\sigma \cdot \Omega_\sigma)}{[\exp(-b_\sigma \cdot \Omega_\sigma) + 1]^2}. \quad (43)$$

The derivatives of J_{sum} to $\Omega_{\sigma_{out}}$ and Ω_{σ_w} in Eq. (39) can be calculated as

$$\frac{\partial J_{sum}}{\partial \Omega_{\sigma_{out}}} = \sum_{x_s} \sum_{y_s} \frac{\partial \mathbf{J}(x_s, y_s)}{\partial \Omega_{\sigma_{out}}}, \quad (44)$$

$$\frac{\partial J_{sum}}{\partial \Omega_{\sigma_w}} = \sum_{x_s} \sum_{y_s} \frac{\partial \mathbf{J}(x_s, y_s)}{\partial \Omega_{\sigma_w}}, \quad (45)$$

where $\partial \mathbf{J}(x_s, y_s) / \partial \Omega_{\sigma_{out}}$ and $\partial \mathbf{J}(x_s, y_s) / \partial \Omega_{\sigma_w}$ are described in Eqs. (41) and (42).

APPENDIX B

In Eq. (22), we have

$$\begin{aligned}
\nabla F|_{\Theta_M} &= a(n_r - n_a) \cdot \mathbf{W}_M^\circ \otimes [\nabla F|_M \\
&\quad \odot \mathbf{M}_M \odot (1 - \mathbf{M}_M)], \quad (46)
\end{aligned}$$

$$\begin{aligned}
\nabla R_d|_{\Theta_M} &= -\frac{8a}{n_r - n_a} \cdot \mathbf{W}_M^\circ \otimes \left[\left(\mathbf{M} - \frac{n_r + n_a}{2} \right) \right. \\
&\quad \left. \odot \mathbf{M}_M \odot (1 - \mathbf{M}_M) \right]. \quad (47)
\end{aligned}$$

In the above two equations, the superscript \circ denotes the rotation of the matrix by 180° in both horizontal and vertical

directions. In addition, $\mathbf{M}_M = \text{sig}\{\mathbf{W}_M \otimes \Theta_M, 1\}$, and $\nabla F|_M$ in Eq. (46) is given by

$$\nabla F|_M = -\frac{2a}{J_{sum}} \sum_{x_s} \sum_{y_s} \mathbf{J}(x_s, y_s) \cdot \text{Re} \left\{ \mathbf{B}^{x_s y_s *} \odot \left[\mathbf{H}^{x_s y_s *} \otimes \left([\mathbf{H}^{x_s y_s} \otimes (\mathbf{B}^{x_s y_s} \odot \mathbf{M})] \otimes \{\mathbf{H}_r^\circ \otimes [\Pi \odot (\tilde{\mathbf{Z}} - \mathbf{Z}) \odot \mathbf{Z} \odot (1 - \mathbf{Z})]\} \right) \right] \right\}. \quad (48)$$

Similarly, in Eq. (23) we have

$$\nabla F|_{\Theta_S} = a(n_r - n_a) \cdot \mathbf{W}_S^\circ \otimes \left[\nabla F|_M \odot \mathbf{M}_S \odot (1 - \mathbf{M}_S) \right], \quad (49)$$

$$\nabla R_d|_{\Theta_S} = -\frac{8a}{n_r - n_a} \cdot \mathbf{W}_S^\circ \otimes \left[\left(\mathbf{M} - \frac{n_r + n_a}{2} \right) \odot \mathbf{M}_S \odot (1 - \mathbf{M}_S) \right]. \quad (50)$$

In the above two equations, $\mathbf{M}_S = \text{sig}\{\mathbf{W}_S \otimes \Theta_S, 1\}$, and $\nabla F|_M$ is described in Eq. (48).

APPENDIX C

In Eq. (26), each element of $\nabla F|_{\Omega_S}$ can be calculated as

$$\frac{\partial F}{\partial \Omega_S(x_s, y_s)} = -2a \cdot \frac{\partial [\mathbf{J}(x_s, y_s)/J_{sum}]}{\partial \Omega_S(x_s, y_s)} \cdot \mathbf{1}_{N \times 1} \cdot \left\{ \left[\mathbf{H}_r \otimes |\mathbf{H}^{x_s y_s} \otimes (\mathbf{B}^{x_s y_s} \odot \mathbf{M})|_2^2 \right] \odot \Pi \odot (\tilde{\mathbf{Z}} - \mathbf{Z}) \odot \mathbf{Z} \odot (1 - \mathbf{Z}) \right\} \cdot \mathbf{1}_{N \times 1}, \quad (51)$$

where $\mathbf{1}_{N \times 1}$ is the one-valued vector, and

$$\frac{\partial [\mathbf{J}(x_s, y_s)/J_{sum}]}{\partial \Omega_S(x_s, y_s)} = \frac{1}{J_{sum}^2} \cdot \left[\frac{\partial \mathbf{J}(x_s, y_s)}{\partial \Omega_S(x_s, y_s)} \cdot J_{sum} - \frac{\partial J_{sum}}{\partial \Omega_S(x_s, y_s)} \cdot \mathbf{J}(x_s, y_s) \right]. \quad (52)$$

In Eq. (52), $\partial \mathbf{J}(x_s, y_s)/\partial \Omega_S(x_s, y_s) = -0.5 \cdot \sin \Omega_S(x_s, y_s)$, and

$$\begin{aligned} \frac{\partial J_{sum}}{\partial \Omega_S(x_s, y_s)} &= \frac{\partial \sum_{x_s} \sum_{y_s} \mathbf{J}(x_s, y_s)}{\partial \Omega_S(x_s, y_s)} \\ &= \frac{\partial \mathbf{J}(x_s, y_s)}{\partial \Omega_S(x_s, y_s)} \\ &= -0.5 \cdot \sin \Omega_S(x_s, y_s). \end{aligned} \quad (53)$$

Thus, Eq. (52) can be simplified as

$$\frac{\partial [\mathbf{J}(x_s, y_s)/J_{sum}]}{\partial \Omega_S(x_s, y_s)} = \frac{1}{J_{sum}^2} \cdot \left[-0.5 \cdot \sin \Omega_S(x_s, y_s) \right] \cdot [J_{sum} - \mathbf{J}(x_s, y_s)]. \quad (54)$$

In Eq. (26), the gradient of source penalty to Ω_S is calculated as [10]

$$\nabla R_S|_{\Omega_S} = \frac{1}{2} a \cdot \text{sig}\{\mathbf{J}, 0\} \odot (1 - \text{sig}\{\mathbf{J}, 0\}) \odot \sin \Omega_S. \quad (55)$$

REFERENCES

- [1] <http://www.itrs2.net/>.
- [2] A. Erdmann, P. Evanschitzky, F. Shao, T. Fühner, G. F. Lorusso, E. Hendrickx, M. Goethals, R. Jonckheere, T. Bret, and T. Hofmann, "Predictive modeling for EUV-lithography: the role of mask, optics, and photoresist effects," in *Proc. SPIE*, vol. 8171, no. 37, pp. 23-33, Oct. 2011.
- [3] B. Wu and A. Kumar, "Extreme ultraviolet lithography: A review," *J. Vac. Sci. Technol. B*, vol. 25, no. 25, pp. 1743-1761, Sep. 2007.
- [4] J. Cain, P. Naulleau, and C. Spanos, "Modeling of EUV photoresists with a resist point spread function," in *Proc. SPIE*, vol. 5751, pp. 1101-1109, May. 2005.
- [5] X. Ma, J. Wang, X. Chen, Y. Li, and G. R. Arce, "Gradient-based inverse extreme ultraviolet lithography," *Appl. Opt.*, vol. 54, no. 24, pp. 7284-300, Aug. 2015.
- [6] H. Song, L. Zavyalova, I. Su, J. Shiely, and T. Schmoeller, "Shadowing effect modeling and compensation for EUV lithography," in *Proc. SPIE*, vol. 7969, p. 79691O, Feb. 2011.
- [7] A. K. Wong, *Resolution Enhancement Techniques in Optical Lithography* (SPIE Press, 2001).
- [8] X. Ma and G. R. Arce, *Computational Lithography*, Wiley Series in Pure and Appl. Opt. (John Wiley and Sons, New York, 2010), 1st ed.
- [9] Y. Li, X. Ma, X. Guo, and L. Dong, "Vectorial resolution enhancement: better fidelity for immersion lithography," SPIE Newsroom, DOI: 10.1117/2.1201409.005461, 2014.
- [10] X. Ma, C. Han, Y. Li, L. Dong, and G. R. Arce, "Pixelated source and mask optimization for immersion lithography," *J. Opt. Soc. Am. A*, vol. 30, no. 1, pp. 112-123, Jan. 2013.
- [11] A. E. Rosenbluth, S. Bukofsky, C. Fonseca, M. Hibbs, K. Lai, A. Molless, R. N. Singh, and A. K. Wong, "Optimum mask and source patterns to print a given shape," *J. Microlith. Microfab. Microsyst.*, vol. 1, no. 1, pp. 13-30, Dec. 2002.
- [12] A. Erdmann, T. Fühner, T. Schnattinger, and B. Tollkühn, "Towards automatic mask and source optimization for optical lithography," in *Proc. SPIE*, vol. 5377, pp. 646-657, May. 2004.
- [13] C. Proglar, W. Conley, B. Socha, and Y. Ham, "Layout and source dependent phase mask transmission tuning," in *Proc. SPIE*, vol. 5454, pp. 315-326, May. 2005.
- [14] S. Robert, X. Shi, and L. David, "Simultaneous source mask optimization (SMO)," in *Proc. SPIE*, vol. 5853, pp. 180-193, Jun. 2005.
- [15] S. Hsu, L. Chen, Z. Li, S. Park, K. Gronlund, H. Liu, N. Callan, R. Socha, and S. Hansen, "An innovative source-mask co-optimization (SMO) method for extending low k_1 imaging," in *Proc. SPIE*, vol. 7140, p. 714010, Dec. 2008.
- [16] X. Ma and G. R. Arce, "Pixel-based simultaneous source and mask optimization for resolution enhancement in optical lithography," *Opt. Express*, vol. 17, no.7, pp. 5783-5793, Mar. 2009.
- [17] Y. Peng, J. Zhang, Y. Wang, and Z. Yu, "Gradient-based source and mask optimization in optical lithography," *IEEE Trans. on Image Proc.*, vol. 20, no. 10, pp. 2856-2864, Oct. 2011.
- [18] J. Yu and P. Yu, "Gradient-based fast source mask optimization (SMO)," in *Proc. SPIE*, vol. 7973, p. 797320, Mar. 2011.
- [19] N. Jia and E. Y. Lam, "Pixelated source mask optimization for process robustness in optical lithography," *Opt. Express*, vol. 19, no. 20, pp. 19384-19398, Sep. 2011.
- [20] J. Li, Y. Shen, and E. Lam, "Hotspot-aware fast source and mask optimization," *Opt. Express*, vol. 20, no. 19, pp. 21792-21804, Sep. 2012.
- [21] S. Li, X. Wang, and Y. Bu, "Robust pixel-based source and mask optimization for inverse lithography," *Optics & Laser Technology*, vol. 45, no. 2, pp. 285-293, Feb. 2013.
- [22] X. Ma, C. Han, Y. Li, B. Wu, Z. Song, L. Dong, and G. R. Arce, "Hybrid source mask optimization for robust immersion lithography," *Appl. Opt.*, vol. 52, no. 18, pp. 4200-4211, May. 2013.
- [23] J. Li, S. Liu, and E. Y. Lam, "Efficient source and mask optimization with augmented Lagrangian methods in optical lithography," *Opt. Express*, vol. 21, no. 7, pp. 8076-8090, Mar. 2013.
- [24] L. Wei and Y. Li, "Hybrid approach for the design of mirror array to produce freeform illumination sources in immersion lithography," *Optik*, vol. 125, no. 20, pp. 6166-6171, Jun. 2014.
- [25] S. Hansen, "Source mask polarization optimization," *J. Micro/Nanolith. MEMS MOEMS*, vol. 10, no. 3, p. 033003, Jul. 2011.
- [26] X. Ma, L. Dong, C. Han, J. Gao, Y. Li, and G. R. Arce, "Gradient-based joint source polarization mask optimization for optical lithography," *J. Micro/Nanolith. MEMS MOEMS*, vol. 14, no. 2, p. 023504, Apr. 2015.
- [27] C. Han, Y. Li, L. Dong, X. Ma, and X. Guo, "Inverse pupil wavefront optimization for immersion lithography," *Appl. Opt.*, vol. 53, no. 29, pp. 6861-6871, Apr. 2014.

- [28] L. Wei, Y. Li, and K. Liu, "Design of freeform illumination sources with arbitrary polarization for immersion lithography," in *Proc. SPIE*, vol. 9272, p. 927221, Nov. 2014.
- [29] T. Fühner, A. Erdmann, and P. Evanschitzky, "Simulation-based EUV source and mask optimization," in *Proc. SPIE*, vol. 7122, p. 71221Y, Oct. 2008.
- [30] P. Evanschitzky, T. Fühner, F. Shao, and A. Erdmann, "Efficient simulation of three dimensional EUV masks for rigorous source mask optimization and mask induced imaging artifact analysis," in *Proc. SPIE*, vol. 7545, p. 75450D, May. 2010.
- [31] X. Liu, R. Howell, S. Hsu, K. Yang, K. Gronlund, F. Driessen, H. Liu, S. Hansen, K. Schenau, T. Hollink, P. Adrichem, K. Troost, J. Zimmermann, O. Schumann, C. Hennerkes, and P. Gräupner, "EUV source-mask optimization for 7 nm node and beyond," in *Proc. SPIE*, vol. 9048, p. 90480Q, Apr. 2014.
- [32] S. Hsu, R. Howell, J. Jia, H. Liu, K. Gronlund, S. Hansen, J. Zimmermann, "EUV resolution enhancement techniques (RETs) for k_1 0.4 and below," in *Proc. SPIE*, vol. 9422, p. 94221I, Mar. 2015.
- [33] R. Kim, O. Wood, M. Crouse, Y. Chen, V. Plachecki, S. Hsu, K. Gronlund, "Application of EUV resolution enhancement techniques (RET) to optimize and extend single exposure bidirectional patterning for 7nm and beyond logic designs," in *Proc. SPIE*, vol. 9776, p. 97761R, Mar. 2016.
- [34] M. Crouse, L. Liebmann, V. Plachecki, M. Salama, Y. Chen, N. Saulnier, D. Dunn, I. Matthew, S. Hsu, K. Gronlund, F. Goodwin, "Design intent optimization at the beyond 7nm node: the intersection of DTCO and EUVL stochastic mitigation techniques," in *Proc. SPIE*, vol. 10148, p. 101480H, Mar. 2017.
- [35] X. Ma, Z. Song, Y. Li, and G. R. Arce, "Block-based mask optimization for optical lithography," *Appl. Opt.*, vol. 52, no. 14, pp. 3351-3363, May. 2013.
- [36] D. Peng, P. Hu, V. Tolani, and T. Dam, "Toward a consistent and accurate approach to modeling projection optics," in *Proc. SPIE*, vol. 7640, p. 76402Y, Mar. 2010.
- [37] T. V. Pistor, A. R. Neureuther, and R. J. Socha, "Modeling oblique incidence effects in photomasks," in *Proc. SPIE*, vol. 4000, pp. 228-237, Jul. 2000.
- [38] M. D. Smith, T. Graves, J. Biafore, S. Robertson, C. Kim, J. Moon, J. Kim, C. Bok, and D. Yim, "Comprehensive EUV lithography model," in *Proc. SPIE*, vol. 7969, p. 796906, Mar. 2011.
- [39] A. Poonawala and P. Milanfar, "Mask design in optical microlithography - an inverse imaging problem," *IEEE Trans. on Image Proc.* vol. 16, no. 3, pp. 774-788, Mar. 2007.
- [40] X. Ma, Y. Li, and L. Dong, "Mask optimization approaches in optical lithography based on a vector imaging model," *J. Opt. Soc. Am. A*, vol. 29, no. 7, pp. 1300-1312, Jun. 2012.
- [41] J. Word, C. Zuniga, M. Lam, M. Habib, K. Adam, and M. Oliver, "OPC modeling and correction solutions for EUV lithography," in *Proc. SPIE*, vol. 8166, p. 81660Q, Oct. 2011.
- [42] G. McIntyre, C. Koay, M. Burkhardt, H. Mizuno, and O. R. Wood, "Modeling and experiments of nontelecentric thick mask effects for EUV lithography," in *Proc. SPIE*, vol. 7271, p. 72711C, Mar. 2009.
- [43] D. Civay, E. Hosler, V. Chauhan, T. G. Neogi, L. Smith, and D. Pritchard, "EUV telecentricity and shadowing errors impact on process margins," in *Proc. SPIE*, vol. 9422, p. 94220Z, Mar. 2015.
- [44] C. G. Krautschik, M. Ito, I. Nishiyama, and K. Otaki, "Impact of the EUV mask phase response on the asymmetry of Bossung curves as predicted by rigorous EUV mask simulations," in *Proc. SPIE*, vol. 4343, pp. 392-401, Aug. 2001.
- [45] P. Yan, "EUVL alternating phase-shift mask imaging evaluation," in *Proc. SPIE*, vol. 4889, pp. 1099-1105, Dec. 2002.
- [46] J. Ruoff, "Impact of mask topography and multilayer stack on high NA imaging of EUV masks," in *Proc. SPIE*, vol. 7823, p. 78231N, Sep. 2010.
- [47] X. Guo, Y. Li, L. Dong, L. Liu, X. Ma, and C. Han, "Parametric source-mask-numerical aperture co-optimization for immersion lithography," *J. Micro/Nanolith. MEMS MOEMS*, vol. 13, no. 4, p. 043013, Nov. 2014.
- [48] J. Nocedal and S. J. Wright, *Numerical Optimization*. 2nd ed. Springer, New York, 2006.
- [49] X. Ma, D. Shi, Z. Wang, Y. Li, and G. R. Arce, "Lithographic source optimization based on adaptive projection compressive sensing," *Opt. Express*, vol. 25, no. 6, pp. 7131-7149, Mar. 2017.
- [50] X. Ma, Z. Wang, Y. Li, G. R. Arce, L. Dong, and J. Garcia-Frias, "Fast optical proximity correction method based on nonlinear compressive sensing," *Opt. Express*, vol. 26, no. 11, pp. 14479-14498, May 2018.
- [51] X. Ma, H. Lin, G. Jiao, Y. Li, and G. R. Arce, "Fast lithographic source optimization using a batch-processing sequential least square estimator," *Appl. Opt.*, vol. 56, no. 21, pp. 5903-5913, Jul. 2017.

- [52] X. Ma, S. Jiang, J. Wang, B. Wu, Z. Song, and Y. Li, "A fast and manufacture-friendly optical proximity correction based on machine learning," *Microelectron. Eng.*, vol. 168, pp. 15-26, 2016.
- [53] X. Ma, S. Jiang, and A. Zakhori, "A cost-driven fracture heuristics to minimize external sliver length," in *Proc. SPIE*, vol. 7973, p. 79732O, Mar. 2011.



Xu Ma received his BS degree in electrical engineering from Tsinghua University, China, and PhD in electrical and computer engineering from the University of Delaware. He was a postdoctoral scholar in electrical engineering and computer sciences at the University of California, Berkeley. He is currently a professor of School of Optoelectronics at Beijing Institute of Technology, Beijing, China. His research interests include computational imaging, image and signal processing based on compressive sensing and deep learning.



Zhiqiang Wang is currently working toward the Ph.D. degree in the optical engineering in Beijing Institute of Technology, Beijing, China. His research interests include lithographic resolution enhancement techniques, particularly source and mask optimization.



Xuanbo Chen is a graduate student in the School of Optoelectronics at Beijing Institute of Technology, Beijing, China. His research interest includes the source and mask optimization methods for EUV lithography systems.



Yanqiu Li received the M.S. and Ph.D. degrees in optics from Harbin Institute of Technology, Harbin, China, in 1996. She was a Senior Engineer at Nikon, as an invited Professor of Tohoku University of Japan, and as a Frontier Researcher at RIKEN, Japan, from 1997 to 2002. She is currently a Professor in the School of Optoelectronics, Beijing Institute of Technology, Beijing, China. She has published numerous articles on lithographic science. Her research interests include advanced lithography technology and optical polarization measurement.



Gonzalo R. Arce is currently the Charles Black Evans Distinguished Professor of electrical and computer engineering with the University of Delaware, Newark, DE, USA. From 2000 to 2009, he has served as a Department Chair. His research interests include computational imaging, coded aperture optimization, and compressive sensing research and development. He was the 2010-2011 Fulbright-Nokia Distinguished Chair in Information and Communications Technologies. He was an elected member of the Arkansas Academy of Engineering. He is a Fellow

of the Center for Advanced Studies, University of Delaware. He has served as an Editor and a Guest-Editor of several scientific journal publications of the IEEE, OSA, and SPIE. He holds 15 US patents and is the author of four books in the areas of imaging and signal processing. He received the J. P. Morgan-Chase Scholar Award, the DuPont Young Investigator Award, and the NSF Research Initiation Award.